



Cooperatively enhanced coking resistance via boron nitride coating over Ni-based catalysts for dry reforming of methane

Jiang Deng^a, Kankan Bu^a, Yongjie Shen^a, Xiaoyu Zhang^a, Jianping Zhang^a,
Kajornsak Faungnawakij^b, Dongsong Zhang^{a,*}

^a International Joint Laboratory of Catalytic Chemistry, State Key Laboratory of Advanced Special Steel, College of Sciences, Shanghai University, 200444 Shanghai, China

^b National Nanotechnology Center, National Science and Technology Development Agency, 111 Thailand Science Park, Pathum Thani 12120, Thailand

ARTICLE INFO

Keywords:

Dry reforming of methane
CO₂ conversion
Ni-based catalysts
Boron nitride
In-situ Raman

ABSTRACT

Dry reforming of methane provides a feasible solution to reduce the greenhouse gas via simultaneously converting CH₄ and CO₂ into useful syngas. However, conventional Ni-based catalysts suffer from deactivation due to serious carbon coking during dry reforming of methane process. Herein, we propose a concept by reducing crystallinity of formed carbon and accelerating carbon oxidation to enhance the coking resistance of Ni-based catalysts. This concept was conducted through a boron nitride coating strategy over reducible oxides supported Ni catalysts, in which the increased carbon diffusion barrier, induced by the boron nitride coating, would lead to more amorphous carbon. While the amorphous carbon was efficiently gasified by active oxygen species derived from reducible oxides. Our findings demonstrate that the coke issues can be solved by building a dynamic carbon removal route.

1. Introduction

Recycling CO₂ and CH₄ to produce syngas (CO, H₂) through dry reforming of methane (DRM) will reduce greenhouse emissions and satisfy the demand for various chemical products [1–4]. Ni-based catalysts are widely explored to catalytic DRM reaction considering their activity and inexpensiveness. However, the extensive carbon deposition would cause the quick deactivation of the catalysts. Usually, the methane decomposition and the Boudouard reaction are the two main reason for the carbon formation and the former one dominate the coke accumulation at elevated temperature (> 700 °C) [5,6]. Accordingly, two effective routes for reducing the carbon formation include inhibition of the Boudouard reaction/CH₄ decomposition and acceleration of the gasification of deposited carbon [7–9].

Normally, coke issue was addressed through the optimization of the supports and active species [10–13]. An effective approach to inhibit the carbon deposition was to passivate the highly reactive step sites of Ni clusters [14–16]. For example, alkaline metals could occupy the step or edge sites of Ni cluster thus suppressed the deep decomposition of methane and alleviated carbon deposition [17–19]. The passivation strategy could achieve the coke resistance at the cost of activity implying

the dilemma between the activity and stability [20]. Recently, the boron nitride was explored as the novel support for Ni-based catalysts to enhance the coke resistance in DRM reaction and the new strong metal-support interactions induced by the reaction was also presented [21–23]. Despite the well coking resistance of BN supported Ni catalysts, the precious mechanism was still controversial. Some researchers proposed the Ni nanoparticle with a small size could effectively inhibit the carbon deposition but also maintain excellent activity, however, the requirement of the specific Ni precursors or complex processes was frustrated [24–26]. Moreover, researchers also proposed single crystal-MgO can serve as the support for Ni-based catalysts which could significantly suppress the carbon deposition [22,27]. However, it still lacked of in situ techniques to unravel the mechanism of coking resistance.

Carbon dioxide was the main oxidant in the reaction gas, whose activation was critical for carbon removal [28,29]. An alternative option was available via increasing the feed ratio of CO₂/CH₄ or storage CO₂ with alkaline earth metal oxide (CaO) [29,30]. Furthermore, reducible metal oxides such as CeO₂ [31–33], ZrO₂ [34], La₂O₃ [34], or their solid solution [35,36] with plentiful oxygen vacancy was favorable for CO₂ activation which was promising as the support for Ni-based catalysts.

* Corresponding author.

E-mail address: dszhang@shu.edu.cn (D. Zhang).

<https://doi.org/10.1016/j.apcatb.2021.120859>

Received 22 July 2021; Received in revised form 23 October 2021; Accepted 25 October 2021

Available online 29 October 2021

0926-3373/© 2021 Elsevier B.V. All rights reserved.

However, plentiful active oxygen species could also contribute to the C-H activation and lead to uncontrollable CH_4 decomposition. For example, the surface adsorbed oxygen species could be regulated by treating with different gas or doping with rare-earth metal and the oxygen species could enhance the DRM reaction [37,38]. Although, the activity of DRM was promoted, the coke issue became severer. Basically, the formed carbon was characterized as amorphous and/or graphitic structure in which the former one was easier to be gasified [39]. The strategy by only optimizing the activation of CO_2 cannot inhibit the carbon deposition effectively because of the sluggish gasification of graphitic carbon.

Generally, the carbon precursors would give rise to carbon atoms which will dissolved into Ni nanoparticles [40]. Subsequently, the carbon would dissolve out and diffuse to the edge or step sites and then give rise to the graphitic carbon [41]. We wonder whether the structure of formed carbon can be controlled via increasing the carbon diffusion barrier rather than the passivation strategy. Hence, we developed a boron nitride (BN) coating strategy and strive to improve the coke resistance of ZrO_2 supported Ni-based catalysts by controlling the structure of formed carbon and accelerating the gasification of coke. The BN was particularly chosen as its well thermostability and chemical inertness. Compared to the oxides with low oxygen storage capacity such as MgO , SiO_2 , and $\gamma\text{-Al}_2\text{O}_3$, ZrO_2 featured well reducibility could enhance the rate of carbon gasification [35]. The higher thermal stability of ZrO_2 compared to CeO_2 also was favorable for DRM reaction with high operation temperature [38]. Based on our density functional (DFT) calculation results, the energy barrier for carbon atom diffusion over BN coated Ni (111) was enhanced. Thus, it was favorable to form amorphous carbon in BN coated catalysts. Moreover, the enhanced CO_2 activation ability also occurred on BN coated catalysts and the derived active oxygen species would facilitate the carbon gasification. As a result, the BN coated catalyst showed great stability with no activity loss during 200 h DRM reaction. This strategy is also applicable to other reducible metal oxides which indicate its potential of wide use.

2. Experiments

2.1. Catalyst preparation

2.1.1. ZrO_2 colloidal sol synthesis

13.0 g KCl was dissolved into 80 mL DI water. $\text{ZrOCl}_2 \cdot 8\text{H}_2\text{O}$ was dissolved into 250 mL DI water. The KCl solution was mixed with ZrOCl_2 solution. The mixture was then put into 500 mL Teflon autoclave and underwent hydrothermal treatment at 180°C for 72 h. 2.4 L HCl (0.1 M) was added into the autoclave after cooling down to the room temperature. The suspension was filtered and the residue was washed until pH = 3.8. Nano ZrO_2 can be obtained after annealing at 400°C for 3 h.

2.1.2. Ni/ ZrO_2 synthesis

1.0 g ZrO_2 was dispersed into 80 mL DI water and 0.55 g Ni $(\text{NO}_3)_2 \cdot 6\text{H}_2\text{O}$ was added then underwent magnetic stirring for 1 h at room temperature. The suspension liquid was vaporized through rotary evaporation at 45°C and dried in the 60°C overnight. The powder was calcined at 400°C for 3 h in air at a ramp rate of $2^\circ\text{C}/\text{min}$ and resulted in NiO/ ZrO_2 . The metal loading was determined by ICP-OES. The NiO/ ZrO_2 was reduced by 10% H_2/N_2 at 30 mL/min at 750°C for an hour at ramp rate of $10^\circ\text{C}/\text{min}$ and give rise to the Ni/ ZrO_2 .

2.1.3. Ni/ ZrO_2 @BN synthesis

1.0 g NiO/ ZrO_2 was dispersed 100 mL DI water, 3.25 g boracic acid and 0.07 g urea was added. The suspension liquid was vaporized through rotary evaporation at 45°C and dried in the 60°C overnight after ultrasonic treatment within 1 h. The powder was calcined at 900°C for 5 h in N_2 at a ramp rate of $5^\circ\text{C}/\text{min}$ and resulted in NiO/ ZrO_2 @BN. The NiO/ ZrO_2 @BN was reduced by 10% H_2/N_2 at 30 mL/min at 750°C for an hour at ramp rate of $10^\circ\text{C}/\text{min}$ and give rise to the Ni/ ZrO_2 @BN.

2.1.4. Ni/ $\gamma\text{-Al}_2\text{O}_3$ synthesis

1.0 g $\gamma\text{-Al}_2\text{O}_3$ was dispersed into 80 mL DI water and 0.55 g Ni $(\text{NO}_3)_2 \cdot 6\text{H}_2\text{O}$ was added then underwent magnetic stirring for 1 h at room temperature. The suspension liquid was vaporized through rotary evaporation at 45°C and dried in the 60°C overnight. The powder was calcined at 550°C for 3 h in air at a ramp rate of $2^\circ\text{C}/\text{min}$ and resulted in NiO/ $\gamma\text{-Al}_2\text{O}_3$. The metal loading was determined by ICP-OES.

2.1.5. Ni/ $\gamma\text{-Al}_2\text{O}_3$ @BN synthesis

1.0 g NiO/ $\gamma\text{-Al}_2\text{O}_3$ was dispersed 100 mL DI water, 3.25 g boracic acid and 0.07 g urea was added. The suspension liquid was vaporized through rotary evaporation at 45°C and dried in the 60°C overnight after ultrasonic treatment within 1 h. The powder was calcined at 900°C for 5 h in N_2 at a ramp rate of $5^\circ\text{C}/\text{min}$ and resulted in NiO/ $\gamma\text{-Al}_2\text{O}_3$ @BN. The NiO/ $\gamma\text{-Al}_2\text{O}_3$ @BN was reduced by 10% H_2/N_2 at 30 mL/min at 750°C for an hour at ramp rate of $10^\circ\text{C}/\text{min}$ and give rise to the Ni/ $\gamma\text{-Al}_2\text{O}_3$ @BN.

2.1.6. LaNiO₃ synthesis

Ni $(\text{NO}_3)_2 \cdot 6\text{H}_2\text{O}$, La $(\text{NO}_3)_3 \cdot 6\text{H}_2\text{O}$ and citric acid (the molar ratio is 1:1:2) were dissolved into solvent (Ethane: H_2O = 30 mL: 10 mL). After stirring for 2 h, the suspension liquid was vaporized through rotary evaporation at 45°C and dried at 60°C overnight. The as-obtained powder was annealed at 400°C for 2 h, and then program to 800°C for 4 h with a ramp rate of $2^\circ\text{C}/\text{min}$. The oxides were reduced by 10% H_2/N_2 at 30 mL/min at 750°C for an hour at ramp rate of $10^\circ\text{C}/\text{min}$ and gave rise to the LaNiO₃. The BN coating procedure is as the same as Ni/ ZrO_2 @BN.

2.2. Characterization of the catalysts

X-ray Diffraction (XRD). X-ray powder diffraction patterns were collected via a Rigaku D/Max-2200 V diffractometer (3KW, Cu K_α as the radiation source, Rigaku, Japan) for $2\theta = 10\text{--}90^\circ$ at a scan rate of $7^\circ/\text{min}$. Transmission Electron Microscopy (TEM). HRTEM and TEM were implemented on a JEM-2100F. The samples were dispersed into the ethanol and then drop cast to the 200 mesh copper grids with carbon film TEM grids for observations.

2.2.1. In situ X-ray diffraction (in situ XRD)

In situ XRD experiments were conducted over Bruker D8 advances diffractometer (3KW, Cu K_α as the radiation source, LYNXEYE_XE.T). The primary soller slit is 4.1° , the secondary soller slit is 4.0° . 20–30 mg catalysts were filled into the reactor (Anton Paar, XRK900). Before the measurement, the catalysts were pretreated at 300°C under N_2 (30 mL/min) for 30 min. The reaction temperature was set at 750°C under N_2 (30 mL/min). Then, the gases ($\text{CH}_4/\text{CO}_2/\text{N}_2 = 10/10/30 \text{ mL}\cdot\text{min}^{-1}$) were injected and the XRD patterns were collected. The N_2 was introduced to dilute the reaction gas and slowed down the rate of carbon deposition which can ensure the enough time to collect informative data.

2.2.2. Temperature-programmed reduction in hydrogen (H_2 -TPR)

H_2 -TPR experiments were carried out on a Micromeritics AutoChem II 2950 instrument. Approximately, the calcined sample before reduction was pretreated in Ar (30 mL/min) at 300°C for 30 min. The sample was heated up to 750°C at $10^\circ\text{C}/\text{min}$ in a 10% H_2/Ar mixture gas flow (30 mL/min).

2.2.3. Temperature-programmed desorption in CO_2 with mass spectra (CO_2 -TPD-MS)

CO_2 -TPD-MS were carried out using a Micromeritics AutoChem II 2920 instrument with on-line mass spectrum (MS, Pfeiffer Omnistar). After reduction, the catalysts were preadsorbed with CO_2 of 50 mL/min at 50°C for 1 h followed by Ar purge at the same temperature for another 30 min to remove physisorbed CO_2 . Temperature programming

was then initiated with a heating rate of 10 °C /min in 50 mL/min of He until 800 °C.

2.2.4. Temperature programmed surface reaction (TPSR)

CH₄-TPSR was carried out using a Micromeritics AutoChem II 2920 instrument connecting with on-line mass spectrum (MS, Pfeiffer Omnistar). The catalysts were reduced in a quartz reactor at 750 °C for 1 h using 10% H₂/Ar with 30 mL/min. The quartz reactor cooled down to the room temperature under the atmosphere of He with 30 mL/min. Then, the pure CH₄ was injected with temperature programming. The temperature of the capillary and injection port is 150 and 120 °C respectively for the online-MS.

2.2.5. Thermal gravimetric analyses (TGA)

TG was tested by NETZSCH STA 449 F1. 10 mg of sample were used in each measurement with heating from room temperature to 900 °C under air atmosphere.

2.2.6. X-ray photoelectron spectroscopy (XPS)

XPS was performed using a RBD upgraded PHI 5000C ESCA system.

2.2.7. In situ diffuse reflectance infrared Fourier transform spectra (in situ DRIFTS)

In situ DRIFTS experiments were carried out on a Nicolet is50 FT-IR spectrometer. For the in situ DRIFTS DRM reaction, the catalyst was pretreated with flowing N₂ at 300 °C for 30 min. Then, the temperature was set at 550 °C and the gases (CH₄/CO₂/N₂ = 10/10/30 mL·min⁻¹) were injected. For the in situ DRIFTS transient reaction of CH₄ and CO₂, the catalysts pre-adsorbed CO₂ (10 mL·min⁻¹) for 1 h and then CH₄ (10 mL·min⁻¹) stream with flowing N₂ (30 mL·min⁻¹) was introduced during the whole test. The reaction temperature was set at 550 °C and the spectra were collected.

2.2.8. In situ Raman spectroscopy

10–20 mg samples were put into the ceramic tube of the Linkam reactor. The Raman experiments were carried out on the LabRAM HR Evolution by using 325 nm laser (The ND filter is 10%, hole value is 100). The spectra were acquired in the range of 1000–2000 cm⁻¹. The spectral resolution employed was 4 cm⁻¹. The in situ Raman was conducted in a gas mixture with CH₄/CO₂/N₂ = 10/10/10 mL/min.

2.2.9. Catalytic activity test

The catalytic activity and stability of the catalysts (120 mg diluted by 0.6 g 20–40 mesh quartz) were conducted in a quartz fixed-bed tubular reactor with a total gas flow rate kept constant at 50 mL/min (CO₂/CH₄ = 25/25 mL/min, GHSV = 25,000 mL·g⁻¹·h⁻¹). The stability was carried out at 750 °C for 200 h. An online GC was equipped with TCD analyzed the products. The conversion of CH₄ and CO₂ (X%) was calculated based on the following equation:

$$X_{\text{CH}_4}(\%) = \frac{[\text{CH}_4]_{\text{in}} - [\text{CH}_4]_{\text{out}}}{[\text{CH}_4]_{\text{in}}}$$

$$X_{\text{CO}_2}(\%) = \frac{[\text{CO}_2]_{\text{in}} - [\text{CO}_2]_{\text{out}}}{[\text{CO}_2]_{\text{in}}}$$

Where [CH₄]_{in} and [CO₂]_{in} are the peak areas of specific species measured by gas chromatography for the blank tube at room temperature. [CH₄]_{out} and [CO₂]_{out} is the peak area of specific species during the DRM reaction.

The H₂/CO ratio of product was determined by:

$$\frac{\text{H}_2}{\text{CO}} = \frac{\text{H}_2 \text{ produced}}{\text{CO produced}}$$

The turnover frequencies (s⁻¹) were calculated according following equation:

$$\text{TOF} = \frac{n_{\text{CH}_4}}{m_{\text{catal}} \times W_{\text{Ni}} \times \frac{D}{M_{\text{Ni}}}}$$

Where n_{CH₄} is molar conversion rate of CH₄, m_{catal} is the weight of catalyst used, W_{Ni} is the mass fraction of Ni in catalysts, D is the metal dispersion determined by H₂-pulse measurement.

2.2.10. Density functional theory (DFT) calculations

Our spin-polarized DFT calculations have been carried out with the Vienna *Ab initio* Simulation Package (VASP) [42] using the Perdew-Burke-Ernzerhof (PBE) [43] functional and the projector augmented wave (PAW) [44] method. For all calculations, a plane wave energy cutoff of 400 eV was used and the Brillouin zone integration was performed using Monkhorst-Pack scheme with 3 × 3 × 1 k-points [45]. For geometry optimizations, the force and energy convergences were 0.02 eV/Å and 10⁻⁶ eV, respectively. In this work, the Ni (111) (4 × 4) slab surface containing 64 Ni atoms was employed. The 0.5 monolayer BN overlayer was composed of 8 B atoms and 8 N atoms and the monolayer BN overlayer consisted of 16 B atoms and 16 N atoms. During geometry optimizations, the bottom 2 Ni layers were fixed to their bulk positions and all the rest atoms were fully relaxed. A vacuum space of 15 Å was added in the direction perpendicular to the surface to prevent interactions between periodic images. In addition, in this study, to understand the migration phenomena and its associated diffusion barriers, the climbing image nudged elastic band (CI-NEB) was applied to locate the diffusion barriers. The adsorption energy (*E*_{ads}) of C on the Ni (111) surface or in BN-nickel interface was defined by *E*_{ads}(C) = *E*_{C/Ni} (or *E*_{C/BN-Ni}) – *E*_{Ni} (or *E*_{BN-Ni}) – *E*_C. Here, *E*_{C/Ni} (or *E*_{C/BN-Ni}), *E*_{Ni} (or *E*_{BN-Ni}) and *E*_C are the energies of adsorption structures, Ni (111) (or BN-Ni (111)) structures and isolated carbon atom, respectively. The activation energy (*E*_a) was calculated to evaluate the diffusion barriers, which was defined by *E*_a = *E*_{TS} – *E*_{IS}. Here, *E*_{TS} and *E*_{IS} are the energies of transient state and initiating state structures.

3. Results and discussion

3.1. Characterization of catalyst

The BN coating process was carried out through the impregnation and subsequent annealing process. The micro-structure of Ni/ZrO₂ and Ni/ZrO₂@BN were characterized through TEM. The pristine ZrO₂ nanoparticles show the random shape with size ranging from 50 to 80 nm (Fig. S1). The loaded Ni nanoparticles form the clumps with the ZrO₂ nanoparticles. After the BN coating process, a BN coating was found over Ni nanoparticles but not the ZrO₂ (Fig. S2). The BN coating might be ascribed to the higher surface energy of Ni nanoparticles because of its much smaller particles size compared to ZrO₂ [46]. The lattice fringe of encapsulated nanoparticle (Fig. 1A) is calculated as 0.20 nm corresponding to the Ni (111) plane. The average lattice distance of ZrO₂ (Fig. 1B Line 2) is 0.158 nm corresponding to the (–222) plane of ZrO₂. The BN layers with interlayer spacing of 0.33 nm and thickness of 2.1 nm were found on Ni nanoparticles (Fig. 1B Line 3). Additionally, some incomplete coating (Fig. S2B) allowed the exposure of Ni which might serve as the active sites for CH₄ activation. Based on the element mapping analysis (Fig. S3A–F), the ZrO₂ proved the framework for the aggregation of Ni, while the B and N appeared around the Ni. The crystal structures of Ni/ZrO₂ and Ni/ZrO₂@BN were characterized by the XRD patterns. As shown in Fig. S4, the XRD patterns of Ni/ZrO₂ are indexed to ZrO₂ (PDF#37-1484) and Ni (PDF#04-0850). However, the content of BN is too low to be detected through XRD. There was negligible change in terms of the full width at half maximum of Ni (111) peaks which suggested no sintering happened at the high temperature treatment (800 °C) during BN coating process. Accordingly, the diameter of Ni over Ni/ZrO₂@BN was as similar as that of Ni/ZrO₂ (Table 1 and Fig. S5). The variations of interaction between Ni

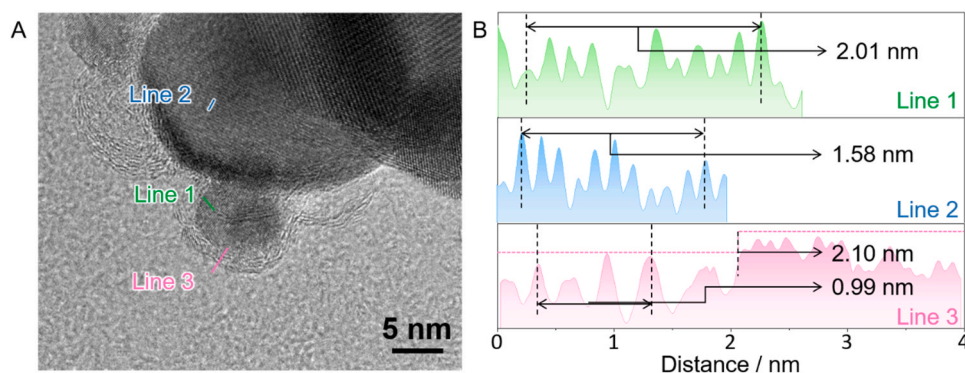


Fig. 1. (A) HRTEM image and (B) the corresponding intensity surface plots of Ni/ZrO₂@BN.

Table 1

Properties of fresh and spent catalysts.

Catalysts	Ni mass loading (wt%) ^a	Metal disperse (%) ^b	Average Particle Size of Ni ^c		I _G /I _D	Grain size of graphitic carbon (nm) ^d
			Fresh catalysts	Spent catalysts		
Ni/ZrO ₂	9.48	4.8	14.3 ± 3.8	22.6 ± 5.2 ^e	1.69	7.44
Ni/ZrO ₂ @BN	7.27	6.1	14.5 ± 5.1	15.4 ± 4.9 ^f	0.93	4.09

^a Data derived from ICP-OES.

^b Data derived from the H₂ pulse measurements at room temperature.

^c The average particle size of Ni was calculated from TEM photos.

^d Results calculated based on Grain size (nm) = 4.4 [I_G/I_D].

^e The spent Ni/ZrO₂ was characterized after 30 h DRM reaction.

^f The spent Ni/ZrO₂@BN was characterized after 200 h DRM reaction.

nanoparticles with support were studied through H₂ temperature programmed reduction (H₂-TPR). The reduction peak (Fig. 2) of Ni/ZrO₂@BN is around 585 °C derived from the transformation from NiO to Ni which is much higher than that of Ni/ZrO₂ indicating a stronger interaction induced by BN coating.

3.2. Performance of catalysts

Prior to the DRM test, the catalysts were treated with 10% H₂/N₂ at 750 °C for 60 min. As shown in Fig. 3A, the initial conversion of CH₄ and CO₂ over Ni/ZrO₂ is 78% and 86%, respectively, and a gradual decline of CH₄ and CO₂ conversion was found with prolonged reaction time. While for the Ni/ZrO₂@BN, the CH₄ and CO₂ conversion kept highly constant during the 50 h DRM reaction. The H₂/CO ratio is around 0.95 for all the catalysts suggesting that reverse water gas reaction gently happened. Note the Ni content in Ni/ZrO₂@BN (7.27 wt%, Table 1) is lower than that in Ni/ZrO₂ (9.48 wt%, Table 1), a higher apparent CH₄ and CO₂

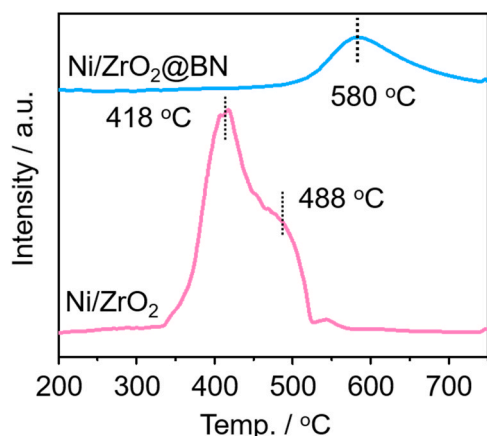


Fig. 2. Plots of TPR profiles for Ni/ZrO₂@BN and Ni/ZrO₂.

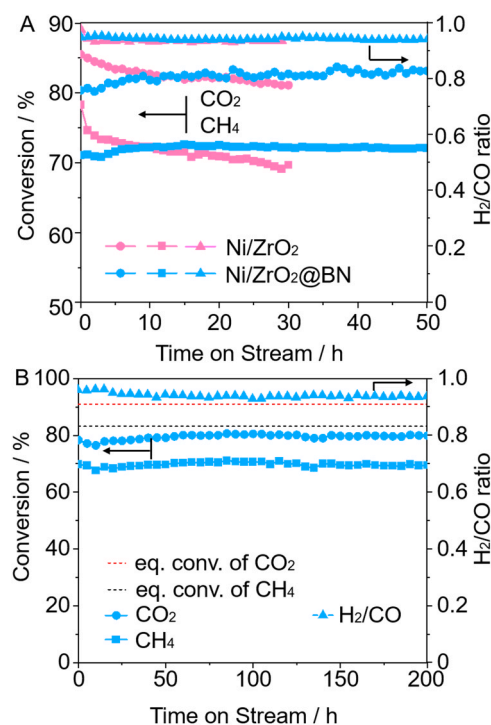


Fig. 3. (A) CH₄, CO₂ conversion and the H₂/CO ratio over Ni/ZrO₂ and Ni/ZrO₂@BN. Conditions: $T = 750\text{ }^{\circ}\text{C}$, CH₄/CO₂ = 1/1, total flow = 50 mL/min (GHSV of 25,000 mL·g_{cat}⁻¹·h⁻¹); (B) CH₄, CO₂ conversion and H₂/CO ratio of Ni/ZrO₂@BN with time on stream of 200 h and the thermodynamic equilibrium conversion of CO₂ and CH₄.

consumption rate was found for Ni/ZrO₂@BN (Fig. S6). Notably, there was negligible activity loss for Ni/ZrO₂@BN after 200 h DRM reaction (Fig. 3B). The robust stability was also better than the BN-nanoceria

interface-confined Ni catalysts reported in our previous report [33]. Hence, the BN coated strategy enables the higher activity and better on-stream stability. The spent catalysts were then characterized by thermogravimetric analysis (TGA) (Fig. 4A) in which only 2.8 wt% coke formed on Ni/ZrO₂@BN even after 200 h DRM reaction. However, a serious carbon deposition occurred to Ni/ZrO₂ with 24.6 wt% deposited carbon after 30 h DRM reaction. The coke formation rate of spent Ni/ZrO₂@BN was 1.9 mg_c·g_{Ni}⁻¹·h⁻¹ which was significantly lower than that of Ni/ZrO₂ (86.7 mg_c·g_{Ni}⁻¹·h⁻¹) (Fig. S7A). Moreover, Ni/ZrO₂@BN exhibited higher turnover frequency of CH₄ (TOF_{CH4}) at 650 °C than that of Ni/ZrO₂ (4.7 vs 2.1 s⁻¹), which is also superior or comparable to other Ni-based catalysts (Fig. S7A and Table S1). Considering both intrinsic activity and coking resistance, Ni/ZrO₂@BN also ranked at the front (Fig. S7A and Table S1) comparing to Ni-based catalysts reported in other literatures. Some catalysts such as Ni/Mg@Al₂O₃ showed initially higher TOF_{CH4} but suffered from serious coking issues and the TOF_{CH4} dropped from 5.3 s⁻¹ to 2.9 s⁻¹ within time on stream of 20 h [24]. The Raman spectra were carried out to explore the properties of the deposited carbon and the intensity of D band (~1400 cm⁻¹) to G band (1590 cm⁻¹) (I_G/I_D) were used to track the graphitic degree of the formed carbon (Fig. S7B and Table 1). The I_G/I_D of spent Ni/ZrO₂@BN 0.93 is much lower than that of catalysts in absence of BN (1.69) (Fig. 4B and Table 1). The crystal size of the deposition carbon calculated based on Raman [47] (Fig. 4B and Table 1) over Ni/ZrO₂@BN is 4.09 nm which is smaller than that of spent Ni/ZrO₂ (8.2 nm). It demonstrated that the deposited carbons on catalysts in absence of BN own more stable structure which might be more difficultly undertaken gasification. The graphitic carbon nanotubes can be also evidenced by scanning electron microscope (SEM) and transmission electron microscope (TEM) photos (Figs. S8 and S9). For the spent Ni/ZrO₂@BN, the graphitic carbon is rarely to be observed. On the other side, the large and mass graphitic carbon nanotubes grow from the spent Ni/ZrO₂. Moreover, the diameter of Ni over spent Ni/ZrO₂@BN after 200 h DRM reaction slightly increased from 14.5 ± 5.1 nm to 15.4 ± 4.9 nm (Table 1 and Fig. S10). However, more serious sintering (14.3 ± 3.8 vs 22.6 ± 5.2) happened to spent Ni/ZrO₂ after 30 h DRM reaction (Table 1 and Fig. S10). To explore the variation of BN layer, the XPS spectra of N 1s and B 1s for Ni/ZrO₂@BN before and after DRM reaction was collected (Fig. S11). The decrease of B 1s and N 1s should be attributed to the partially coverage of carbon after the DRM reaction. The more distinct decrease of intensity for N 1s suggested the BN might be partially etched during the DRM reaction [23]. To explore the properties of deposited carbon, the photoelectron spectra of C 1s were collected (Fig. S12). The content of sp²-C in spent Ni/ZrO₂@BN was 36.3% which was lower than that of spent Ni/ZrO₂ (52.5%) which was consistent with the Raman results. The spent Ni/ZrO₂@BN was further characterized by HRTEM (Fig. S13) in which the BN layer still existed but with the thinner thickness. The Based on the experimental results above, the Ni/ZrO₂@BN exhibited

higher intrinsic activity, less sintering issue, robust stability, and much better coke resistance than Ni/ZrO₂. Moreover, the formed coke in spent Ni/ZrO₂@BN featured less graphitic property.

3.3. In situ XRD measurements

Basically, the CH₄ undertake completed decomposition, then the derived C* will dissolve into the Ni crystal lattice and will give rise to the graphitic carbon via saturated precipitation [48]. The in situ XRD was used to measure the lattice variation of Ni over Ni/ZrO₂ and Ni/ZrO₂@BN (Fig. 5). With the introduction of reaction gases (CH₄, CO₂), the Ni (111) peak in both Ni/ZrO₂@BN and Ni/ZrO₂ moved to lower diffraction angle indicating Ni lattice expanding (Fig. 5A) which should attribute to the insertion of the carbon [49]. With the proceeding of DRM reaction, the Ni (111) peak in both Ni/ZrO₂@BN and Ni/ZrO₂ shifted back which was attributed the exsolution of carbon. The slightly change of the peak position of Ni (111) over Ni/ZrO₂@BN suggested less carbon formation compared with Ni/ZrO₂. The lattice variation was calculated via Bragg equation for a better comparison (Fig. 5B). The decline of lattice distance at direction of Ni (111) for Ni/ZrO₂@BN at 30 min was caused by exsolution of carbon. Subsequently, the increase of lattice distance suggested the carbon derived from CH₄ decomposition further inserted into the lattice of Ni. Because of the efficient carbon removal in Ni/ZrO₂@BN, the accumulation of carbon was inhibited. The decline of lattice distance at direction of Ni (111) for Ni/ZrO₂@BN happened again at 60 min. The increase and decrease of the lattice distance happened periodically demonstrating sequential carbon dissolution and exsolution occurred over Ni/ZrO₂@BN. The lattice distance at direction of Ni (111) decreased slightly at 20 min for Ni/ZrO₂ suggested the exsolution carbon was not distinct. However, the subsequent increase of lattice distance indicated the carbon further inserted into the Ni lattice. The remarkably decrease of lattice distance of Ni in 50 min demonstrated large amount of carbon exsolved. Compared to Ni/ZrO₂@BN, Ni/ZrO₂ shows larger lattice expanding suggesting more carbon dissolved into the Ni (Fig. 5B and the inset). Eventually, the XRD pattern cannot be observed at the prolonged reaction time due to the serious carbon deposition over Ni/ZrO₂. Based on the results of in-situ XRD, the sluggish removal of carbon in Ni/ZrO₂ cannot maintain the dynamic balance between carbon formation and removal which would give rise to the serve carbon disposition.

3.4. In situ Raman spectroscopic measurement

To further explore the dynamics of the carbon formation and removal, in situ Raman spectroscopy was used to identify the deposited carbon during the DRM reaction over Ni/ZrO₂@BN and Ni/ZrO₂. It should be note that the D band is negligible over Ni/ZrO₂@BN because of the quick removal of the amorphous carbon with CO₂ (Figs. 6A and

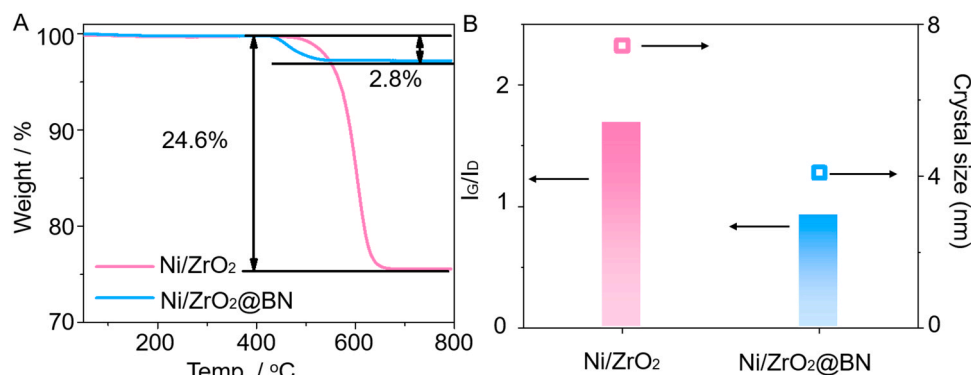


Fig. 4. (A) TG analysis results of spent catalysts in which the spent Ni/ZrO₂ and Ni/ZrO₂@BN was collected after 30 h and 200 h DRM reaction, respectively; (B) I_G/I_D and the crystalline size of deposited carbon over spent catalysts.

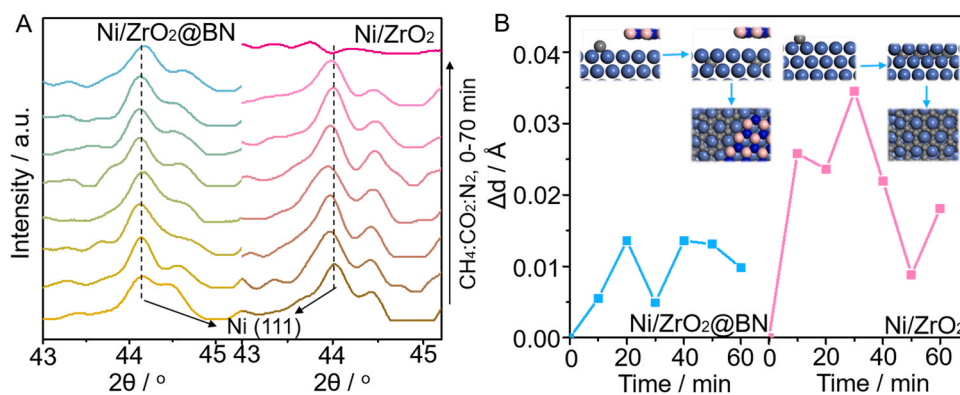


Fig. 5. In situ XRD patterns of (A) Ni/ZrO₂@BN and Ni/ZrO₂ collected at 750 °C under the atmosphere of CH₄/CO₂/N₂ = 1/1/3 with total flow of 50 mL/min for 70 min; and (B) the variation of the lattice distance at direction of Ni (111) and the corresponding schematic diagram during the in situ XRD measurements.

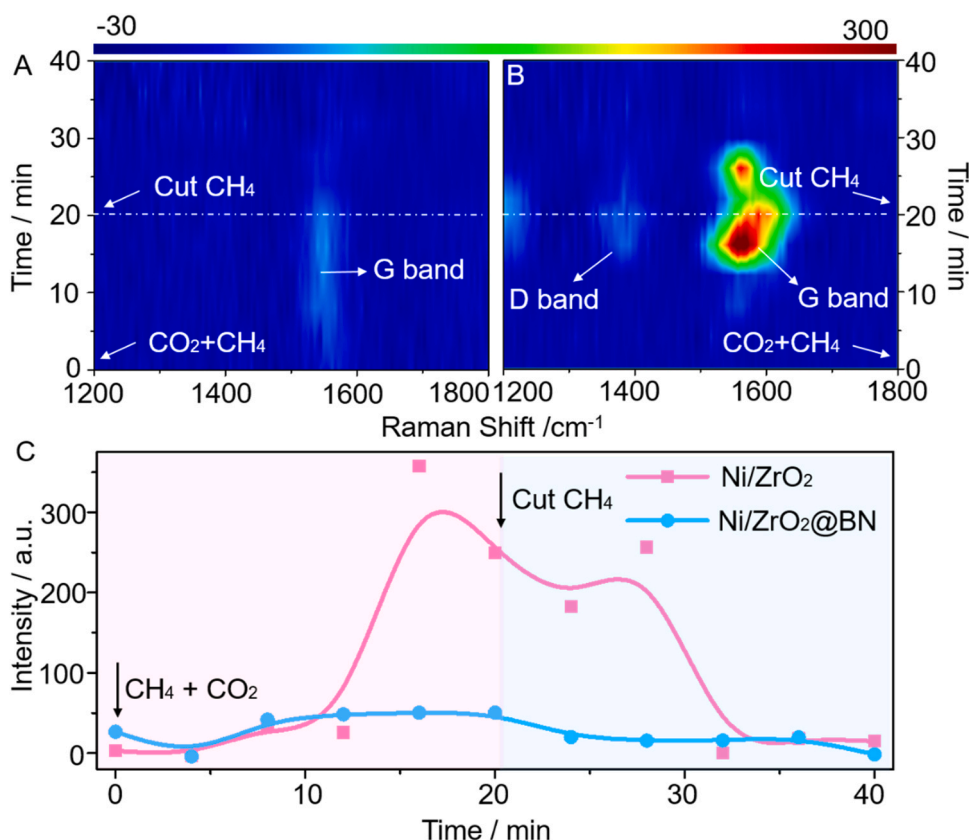


Fig. 6. In situ Raman spectra of (A) Ni/ZrO₂@BN and (B) Ni/ZrO₂ with CH₄/CO₂/N₂ = 1/1/1 with total flow of 30 mL/min for the first 20 min, then the CH₄ was cut off for the rest 20 min; and (C) the variation of G band intensity over Ni/ZrO₂@BN and Ni/ZrO₂ based on in situ Raman spectra results.

S14). The G band at around 1540 cm⁻¹ ascribable to the graphitic carbon quickly emerged at the first 8 min for both Ni/ZrO₂@BN and Ni/ZrO₂ (Fig. 6A and B). Different from Ni/ZrO₂@BN whose G band remains stable along the DRM reaction, the G band of Ni/ZrO₂ increased continually indicating the more serious carbon deposition (Fig. 6C). The more stable coke in the spent Ni/ZrO₂ was also confirmed by the results of O₂-TPO for the spent catalysts (Fig. S15). The constant intensity of the G band of Ni/ZrO₂@BN suggested the dynamic balance between carbon formation and removal which was consistent with the results of in situ XRD. Theoretically, the graphitic carbon can be oxidized by CO₂ thermodynamically when the temperature was higher than 708 °C as calculated. The CH₄ was then turn off and the G band intensity of Ni/ZrO₂@BN decreased instantly while it took 12 min to remove the carbon over Ni/ZrO₂ (Fig. 6C) which suggested more quick carbon removal over

Ni/ZrO₂@BN. Based on the in situ Raman results, the BN layer in Ni/ZrO₂@BN would inhibit the formation of graphitic carbon. Also, the deposited carbon can be thoroughly removed with abundant CO₂, and obviously, the carbon deposition rate is beyond the gasification rate for Ni/ZrO₂.

3.5. DFT calculations

The plane surfaces of bare Ni nanoparticle are modeled by the close-packed Ni (111) surface of four-layer slabs with p (4 × 4) unit cells. The carbon atom located at hollow site with adsorption energy of -7.0 eV. The carbon diffusion barrier was calculated as 0.21 eV from one hollow site to another one (Fig. 7A). The BN-nickel interface is modeled by a Ni (111) surface with 0.5 monolayer BN overlayer. The BN overlayer is

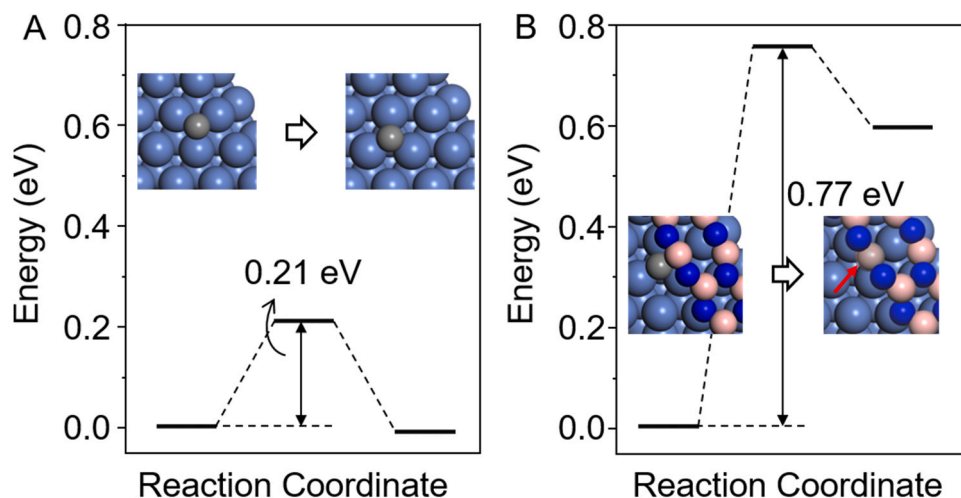


Fig. 7. DFT calculation results of carbon diffusion over different models. (A) carbon diffusion on Ni (111); and (B) carbon diffusion on Ni (111) covered by 0.5 monolayer BN.

bound to the nickel surface through the strong chemical adsorption as the adsorption energy of BN over Ni (111) was calculated as 0.053 eV (Fig. S16). The adsorption energy of carbon over hollow site in the interface is -5.84 eV which is weaker than the counterparts in bare Ni (111). The diffusion energy barrier is 0.77 eV (Fig. 7B) when the carbon diffused from hollow sites of Ni to BN overlaid sites which suggested the carbon diffusion would be difficult on the BN covered Ni. Because of the BN layer, the carbon diffusion needed overcome the extra barrier caused by the BN. The high energy diffusion barrier would lead to less graphitic structure [50]. Also, the BN layer can stabilize the sublayered carbon making it difficult to exsolution (Fig. S17). The DFT calculation results indicated the BN coated Ni (111) was not favorable for carbon accumulation and formed the graphitic carbon on the surface.

3.6. Surface properties and TPSR

The O 1s spectrum of Ni/ZrO₂@BN clearly evidenced the presence of two types of O where the O_α located at higher BE corresponds to the

active adsorbed O and the O_β at the lower BE is the lattice O (Fig. 8). The O_α percentage in Ni/ZrO₂@BN is 35.4% which is higher than Ni/ZrO₂ (14.9%). Moreover, the O_α can serve as the oxidant that can remove deposition carbon and empower Ni/ZrO₂@BN the faster gasification capability than Ni/ZrO₂. The active adsorbed O derived from the redox metal oxides is important for the coke removal. When the ZrO₂ was replaced by the LaNiO₃, the BN coated catalysts show the similar positive effect (Figs. S18 and S19). However, when replacing ZrO₂ with Al₂O₃, the coke issue is still not alleviated (Figs. S20 and S21) even with higher I_G/I_D. Moreover, the results from the temperature programmed desorption of CO₂ combined with mass spectra (CO₂-TPD-MS) show the main CO₂ desorption peak position at 499 °C over Ni/ZrO₂@BN which is higher than that of Ni/ZrO₂ (387 °C) signifying a stronger adsorption towards CO₂ (Fig. 8B and C). Additionally, the CO₂ MS signal of Ni/ZrO₂@BN was higher than that of Ni/ZrO₂ which suggested the higher desorption amount of CO₂. According to the results of CO₂-TPD-MS, CO emerged at 480 °C for Ni/ZrO₂@BN. While the CO MS signal output at 422 °C for Ni/ZrO₂. Because of the continuous release of CO above

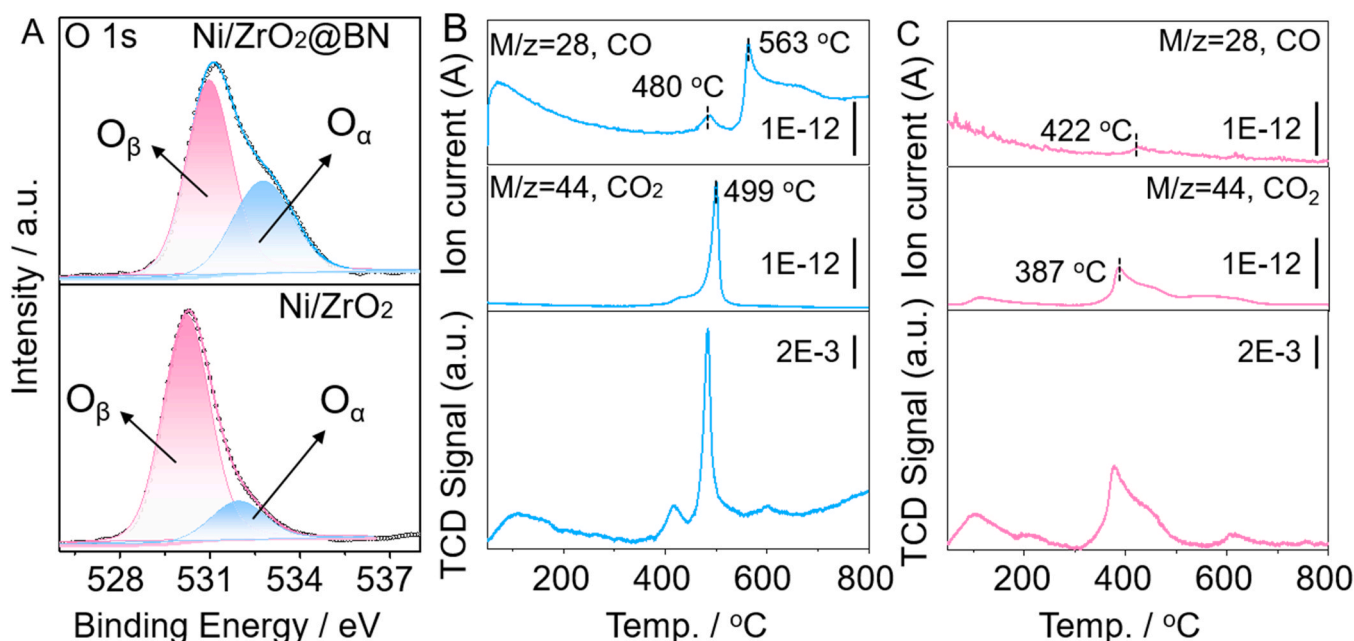


Fig. 8. (A) XPS spectra of O 1s over the Ni/ZrO₂@BN and Ni/ZrO₂; CO₂-TPD-MS of (B) Ni/ZrO₂@BN and (C) Ni/ZrO₂.

563 °C (Fig. 8B) for Ni/ZrO₂@BN, Ni/ZrO₂@BN showed a stronger CO₂ adsorption which would facilitate the DRM reaction at high temperature. The CH₄-TPSR was further conducted as shown in Fig. S22. The lower initial CH₄ decomposition temperature (390 °C) over Ni/ZrO₂ compared to Ni/ZrO₂@BN (495 °C) suggested the activation of CH₄ in Ni/ZrO₂@BN was inhibited compared to Ni/ZrO₂. Because of the better activation of both CH₄ and CO₂, Ni/ZrO₂ showed a better initial DRM performance than that of Ni/ZrO₂@BN. However, the continuous decline of activity for Ni/ZrO₂ caused by the severe carbon decomposition led to a poor stability. According to CO₂-TPD-MS results, Ni/ZrO₂@BN showed stronger adsorption of CO₂ and was able to activate CO₂ at lower temperature which was favorable for carbon removal. Additionally, active adsorbed O derived from the redox metal oxides is vital to maintain the dynamic balance between carbon deposition and removal.

3.7. Reaction mechanism

In order to understand the DRM reaction mechanism, in situ diffuse reflectance infrared Fourier transform spectroscopy (DRIFTS) experiment was carried over Ni/ZrO₂@BN by flowing both CH₄ and CO₂. According to Figs. 9A and S23, the monodentate formate located at 1602 cm⁻¹ [51] emerged at 20 s and the peak intensity increased with reaction time. Subsequently, the CO peak appeared at 30 s and the intensity of CO peak increased with the proceeding of reaction. The bicarbonate came out at 40 s and quickly disappeared with the reaction time suggesting the efficient conversion from bicarbonate to bidentate formate. Meanwhile, the decrease of monodentate carbonate was sluggish compared to bicarbonate and the peak of monodentate carbonate was still observed at 60 s. Furthermore, the transient state experiment with pre-adsorption of CO₂ and followed by CH₄ flowing was carried out. The background was collected after pre-adsorption of CO₂ in which the negative peaks derived from the consumption species and the positive peaks came from the as-formed new species. As exhibited in Figs. 9B and S24, the cumulative of both bicarbonate formate and monodentate suggested the strong adsorption of CO₂ corresponding to the CO₂-TPD-MS results. With flowing of CH₄, the bicarbonate carbonate was consumed and the bidentate formate emerged accordingly. In contrast, the monodentate carbonate could be still observed at 60 s which also suggested the inefficient conversion of monodentate.

Based on the in-situ DRIFTS results, the possible reaction mechanism over Ni/ZrO₂@BN was clarified as shown in Fig. 10. Firstly, CO₂ will be activated by the catalysts and give rise to the O* and CO*. Subsequently, CH₄ undergo the decomposition over Ni and the resulted CH₂* will react with O* and produce the formate. Additionally, the O* will also react with CO₂* and give rise to the bidentate carbonate or monodentate carbonate. The carbonate will react with H* and form formate after dehydration where the conversion of bicarbonate is more efficiently.

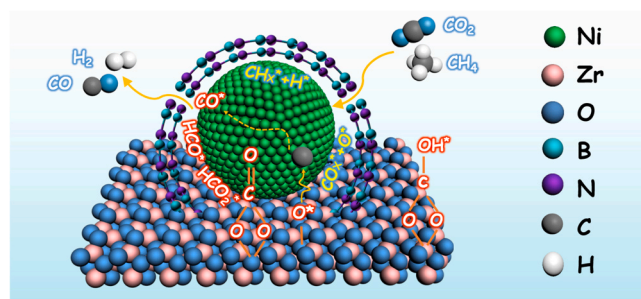


Fig. 10. schematic illustration of the possible reaction mechanism over Ni/ZrO₂@BN based on in situ DRIFTS results and in situ Raman results.

The formate was regarded as the important intermediates for DRM reaction, as it will decompose into H₂ and CO [21,22]. The C* derived from the fully decomposition of CH₄ would accumulate on the surface of the catalysts. More amorphous structure would be formed with BN coating. Furthermore, the O* derived from the reducible oxides would contribute to the gasification of formed carbon and give rise to CO or CO₂, which maintained the dynamic balance between carbon deposition and carbon removal.

4. Conclusion

In summary, the coke issue in DRM has been addressed through the BN coating and cooperation with reducible oxide support. The BN layer can improve the energy barrier for C* migration which resulted in more amorphous carbon. The enhanced CO₂ adsorption and activation after BN coating will accelerate the gasification of carbon. Hence, the dynamic balance of carbon formation and removal will efficiently suppress the carbon accumulation over Ni/ZrO₂@BN. As a result, the Ni/ZrO₂@BN shows robust stability with no activity loss after 200 h DRM reaction. Moreover, the BN coating strategy was applied to other reducible metal oxides proving its universality. Our research results provide the novel strategy to solve the coke issue which can be applicable widely to other methane conversion reactions.

CRediT authorship contribution statement

Jiang Deng: Investigation, Writing – original draft. **Kankan Bu:** Investigation. **Yongjie Shen:** Investigation. **Xiaoyu Zhang:** Investigation. **Jianping Zhang:** Writing – review & editing. **Kajornsak Faungnawakij:** Writing – review & editing. **Dengsong Zhang:** Conceptualization, Supervision, Writing – review & editing, Funding acquisition.

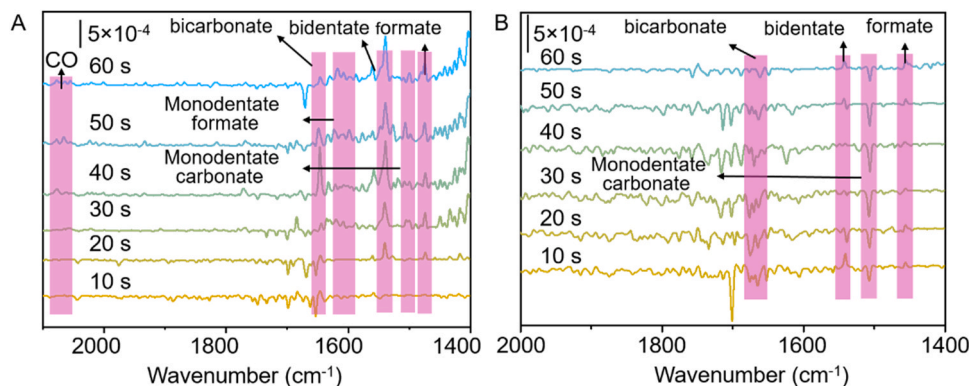


Fig. 9. (A) in situ DRIFT spectra of DRM reaction and (B) in situ DRIFT spectra of transient state reaction with pre-adsorption of CO₂ for 1 h and subsequent CH₄ flowing and over Ni/ZrO₂@BN; the background was collected after pre-adsorption of CO₂.

Declaration of Competing Interest

The authors declare that they have no known competing financial interests or personal relationships that could have appeared to influence the work reported in this paper.

Acknowledgments

This work was financially supported by the National Key R&D Program of China (2017YFE0132400). We also thank for the computing time in Shanghai Supercomputer Center.

Appendix A. Supporting information

Supplementary data associated with this article can be found in the online version at [doi:10.1016/j.apcatb.2021.120859](https://doi.org/10.1016/j.apcatb.2021.120859).

References

- [1] C. Palmer, D.C. Upham, S. Smart, M.J. Gordon, H. Metiu, E.W. McFarland, Dry reforming of methane catalysed by molten metal alloys, *Nat. Catal.* 3 (2020) 83–89.
- [2] L.C. Buelens, V.V. Galvita, H. Poelman, C. Detavernier, G.B. Marin, Super-dry reforming of methane intensifies CO₂ utilization via Le Chatelier's principle, *Science* 354 (2016) 449–452.
- [3] S.D. Angeli, S. Gossler, S. Lichtenberg, G. Kass, A.K. Agrawal, M. Valerius, K. P. Kinzel, O. Deutschmann, Reduction of CO₂ emission from off-gases of steel industry by dry reforming of methane, *Angew. Chem. Int. Ed.* 60 (2021) 11852–11857.
- [4] I.V. Yentekakis, P. Panagiotopoulou, G. Artemakis, A review of recent efforts to promote dry reforming of methane (DRM) to syngas production via bimetallic catalyst formulations, *Appl. Catal. B: Environ.* 296 (2021), 120210.
- [5] M. Akri, S. Zhao, X. Li, K. Zang, A.F. Lee, M.A. Isaacs, W. Xi, Y. Gangarajula, J. Luo, Y. Ren, Y.-T. Cui, L. Li, Y. Su, X. Pan, W. Wen, Y. Pan, K. Wilson, L. Li, B. Qiao, H. Ishii, Y.-F. Liao, A. Wang, X. Wang, T. Zhang, Atomically dispersed nickel as coke-resistant active sites for methane dry reforming, *Nat. Commun.* 10 (2019) 5181.
- [6] N.D. Charisiou, S.L. Douvartzides, G.I. Siakavelas, L. Tzounis, V. Sebastian, V. Stolojan, S.J. Hinder, M.A. Baker, K. Polychronopoulou, M.A. Goula, The relationship between reaction temperature and carbon deposition on nickel catalysts based on Al₂O₃, ZrO₂ or SiO₂ supports during the biogas dry reforming reaction, *Catalysts* 9 (2019) 676.
- [7] S.A. Theofanidis, V.V. Galvita, H. Poelman, G.B. Marin, Enhanced carbon-resistant dry reforming Fe-Ni catalyst: role of Fe, *ACS Catal.* 5 (2015) 3028–3039.
- [8] S.M. Kim, P.M. Abdala, T. Margossian, D. Hosseini, L. Foppa, A. Armutlulu, W. van Beek, A. Comas-Vives, C. Copéret, C. Mueller, Cooperativity and dynamics increase the performance of NiFe dry reforming catalysts, *J. Am. Chem. Soc.* 139 (2017) 1937–1949.
- [9] S. Zhang, M. Ying, J. Yu, W. Zhan, L. Wang, Y. Guo, Y. Guo, Ni_xAl_{1-x}O₂₋₃ mesoporous catalysts for dry reforming of methane: the special role of NiAl₂O₄ spinel phase and its reaction mechanism, *Appl. Catal. B: Environ.* 291 (2021), 120074.
- [10] Y. Tang, Y. Wei, Z. Wang, S. Zhang, Y. Li, L. Nguyen, Y. Li, Y. Zhou, W. Shen, F. F. Tao, P. Hu, Synergy of single-atom Ni₁ and Ru₁ sites on CeO₂ for dry reforming of CH₄, *J. Am. Chem. Soc.* 141 (2019) 7283–7293.
- [11] S.A. Theofanidis, R. Batchu, V.V. Galvita, H. Poelman, G.B. Marin, Carbon gasification from Fe-Ni catalysts after methane dry reforming, *Appl. Catal. B: Environ.* 185 (2016) 42–55.
- [12] B. Yang, J. Deng, H. Li, T. Yan, J. Zhang, D. Zhang, Coking-resistant dry reforming of methane over Ni/γ-Al₂O₃ catalysts by rationally steering metal-support interaction, *iScience* 24 (2021), 102747.
- [13] Y. Lu, D. Guo, Y. Zhao, Y. Zhao, S. Wang, X. Ma, Enhanced performance of xNi@yMo-HSS catalysts for DRM reaction via the formation of a novel SiMoO_x species, *Appl. Catal. B: Environ.* 291 (2021), 120075.
- [14] A. Fouskas, M. Kollia, A. Kambolis, C. Papadopolou, H. Matralis, Boron-modified Ni/Al₂O₃ catalysts for reduced carbon deposition during dry reforming of methane, *Appl. Catal. A-Gen.* 474 (2014) 125–134.
- [15] R. Franz, T. Kühlewind, G. Shter, E. Abou-Hamad, A. Parastaev, E. Uslamin, E.J. M. Hensen, F. Kapteijn, J. Gascon, E.A. Pidko, Impact of small promoter amounts on coke structure in dry reforming of methane over Ni/ZrO₂, *Catal. Sci. Tech.* 10 (2020) 3965–3974.
- [16] S. Chen, J. Zaffran, B. Yang, Descriptor design in the computational screening of Ni-based catalysts with balanced activity and stability for dry reforming of methane reaction, *ACS Catal.* 10 (2020) 3074–3083.
- [17] S. Dama, S.R. Ghodke, R. Bobade, H.R. Gurav, S. Chilukuri, Active and durable alkaline earth metal substituted perovskite catalysts for dry reforming of methane, *Appl. Catal. B: Environ.* 224 (2018) 146–158.
- [18] J. Juan-Juan, M.C. Roman-Martinez, M.J. Illan-Gomez, Effect of potassium content in the activity of K-promoted Ni/Al₂O₃ catalysts for the dry reforming of methane, *Appl. Catal. A-Gen.* 301 (2006) 9–15.
- [19] A.E.C. Luna, M.E. Iriarte, Carbon dioxide reforming of methane over a metal modified Ni-Al₂O₃ catalyst, *Appl. Catal. A-Gen.* 343 (2008) 10–15.
- [20] X. He, Y. Deng, Y. Zhang, Q. He, D. Xiao, M. Peng, Y. Zhao, H. Zhang, R. Luo, T. Gan, H. Ji, D. Ma, Mechanochemical kilogram-scale synthesis of noble metal single-atom catalysts, *Cell Rep. Phys. Sci.* 1 (2020), 100004.
- [21] Y. Cao, P. Maitarad, M. Gao, T. Taketsugu, H. Li, T. Yan, L. Shi, D. Zhang, Defect-induced efficient dry reforming of methane over two-dimensional Ni/h-boron nitride nanosheet catalysts, *Appl. Catal. B: Environ.* 238 (2018) 51–60.
- [22] K. Bu, J. Deng, X. Zhang, S. Kuboon, T. Yan, H. Li, L. Shi, D. Zhang, Promotional effects of B-terminated defective edges of Ni/boron nitride catalysts for coking- and sintering-resistant dry reforming of methane, *Appl. Catal. B: Environ.* 267 (2020), 118692.
- [23] J. Dong, Q. Fu, H. Li, J. Xiao, B. Yang, B. Zhang, Y. Bai, T. Song, R. Zhang, L. Gao, J. Cai, H. Zhang, Z. Liu, X. Bao, Reaction-induced strong metal-support interactions between metals and inert boron nitride nanosheets, *J. Am. Chem. Soc.* 142 (2020) 17167–17174.
- [24] T. Margossian, K. Larmier, S.M. Kim, F. Krumeich, A. Fedorov, P. Chen, C. R. Müller, C. Copéret, Molecularly tailored nickel precursor and support yield a stable methane dry reforming catalyst with superior metal utilization, *J. Am. Chem. Soc.* 139 (2017) 6919–6927.
- [25] D. Baudouin, K.C. Szeto, P. Laurent, A. De Mallmann, B. Fenet, L. Veyre, U. Rodemerck, C. Copéret, C. Thieuleux, Nickel-silicide colloid prepared under mild conditions as a versatile Ni precursor for more efficient CO₂ reforming of CH₄ catalysts, *J. Am. Chem. Soc.* 134 (2012) 20624–20627.
- [26] C.M. Damaskinos, J. Zavanik, P. Djinić, A.M. Efstathiou, Dry reforming of methane over Ni/Ce_{0.8}Ti_{0.2}O₂₋₃: The effect of Ni particle size on the carbon pathways studied by transient and isotopic techniques, *Appl. Catal. B: Environ.* 296 (2021), 120321.
- [27] F. Cheng, X. Duan, K. Xie, Dry reforming of CH₄/CO₂ by stable Ni nanocrystals on porous single-crystalline MgO monoliths at reduced temperature, *Angew. Chem. Int. Ed.* 60 (2021) 18792–18799.
- [28] K. Yuan, J.-Q. Zhong, X. Zhou, L. Xu, S.L. Bergman, K. Wu, G.-Q. Xu, S.L. Bernasek, H.X. Li, W. Chen, Dynamic oxygen on surface: catalytic intermediate and coking barrier in the modeled CO₂ reforming of CH₄ on Ni (111), *ACS Catal.* 6 (2016) 4330–4339.
- [29] P. Wu, Y. Tao, H. Ling, Z. Chen, J. Ding, X. Zeng, X. Liao, C. Stampfl, J. Huang, Cooperation of Ni and CaO at interface for CO₂ reforming of CH₄: a combined theoretical and experimental study, *ACS Catal.* 9 (2019) 10060–10069.
- [30] S. Tian, F. Yan, Z. Zhang, J. Jiang, Calcium-looping reforming of methane realizes in situ CO₂ utilization with improved energy efficiency, *Sci. Adv.* 5 (2019) eaav5077.
- [31] Z. Liu, D.C. Grinter, P.G. Lustemberg, T.-D. Nguyen-Phan, Y. Zhou, S. Luo, I. Waluyo, E.J. Crumlin, D.J. Stacchiola, J. Zhou, J. Carrasco, H.F. Busnengo, M. V. Ganduglia-Pirovano, S.D. Senanayake, J.A. Rodriguez, Dry reforming of methane on a highly-active Ni-CeO₂ catalyst: effects of metal-support interactions on C-H bond breaking, *Angew. Chem. Int. Ed.* 55 (2016) 7455–7459.
- [32] M. Li, A.C. van Veen, Tuning the catalytic performance of Ni-catalysed dry reforming of methane and carbon deposition via Ni-CeO_{2-x} interaction, *Appl. Catal. B: Environ.* 237 (2018) 641–648.
- [33] M. Lu, X. Zhang, J. Deng, S. Kuboon, K. Faungnawakij, S. Xiao, D. Zhang, Coking-resistant dry reforming of methane over BN-nanoceria interface-confined Ni catalysts, *Catal. Sci. Tech.* 10 (2020) 4237–4244.
- [34] A. Löfberg, J. Guerrero-Caballero, T. Kane, A. Rubbens, L. Jalowiecki-Duhamel, Ni/CeO₂ based catalysts as oxygen vectors for the chemical looping for reforming of methane for syngas production, *Appl. Catal. B: Environ.* 212 (2017) 159–174.
- [35] A.L.A. Marinho, R.C. Rabelo-Neto, F. Epron, N. Bion, F.S. Toniolo, F.B. Noronha, Embedded Ni nanoparticles in CeZrO₂ as stable catalyst for dry reforming of methane, *Appl. Catal. B: Environ.* 268 (2020), 118387.
- [36] B. Savavinia, Y. Wang, C. Jiang, C. Roman, P. Darapaneni, J. Larrivière, D. A. Cullen, K.M. Dooley, J.A. Dorman, Enhancing Ce₂Zr_{1-x}O₂ activity for methane dry reforming using subsurface Ni dopants, *ACS Catal.* 10 (2020) 4070–4079.
- [37] M. Zhang, J. Zhang, Z. Zhou, S. Chen, T. Zhang, F. Song, Q. Zhang, N. Tsubaki, Y. Tan, Y. Han, Effects of the surface adsorbed oxygen species tuned by rare-earth metal doping on dry reforming of methane over Ni/ZrO₂ catalyst, *Appl. Catal. B: Environ.* 264 (2020), 118522.
- [38] M. Zhang, J. Zhang, Y. Wu, J. Pan, Q. Zhang, Y. Tan, Y. Han, Insight into the effects of the oxygen species over Ni/ZrO₂ catalyst surface on methane reforming with carbon dioxide, *Appl. Catal. B: Environ.* 244 (2019) 427–437.
- [39] I.V. Yentekakis, P. Panagiotopoulou, G. Artemakis, A review of recent efforts to promote dry reforming of methane (DRM) to syngas production via bimetallic catalyst formulations, *Appl. Catal. B: Environ.* 296 (2021), 120210.
- [40] Y. Bai, H. Yue, J. Wang, B. Shen, S. Sun, S. Wang, H. Wang, X. Li, Z. Xu, R. Zhang, F. Wei, Super-durable ultralong carbon nanotubes, *Science* 369 (2020) 1104–1106.
- [41] R. Zhang, Y. Zhang, F. Wei, Horizontally aligned carbon nanotube arrays: growth mechanism, controlled synthesis, characterization, properties and applications, *Chem. Soc. Rev.* 46 (2017) 3661–3715.
- [42] G. Kresse, J. Furthmüller, Efficient iterative schemes for ab initio total-energy calculations using a plane-wave basis set, *Phys. Rev. B* 54 (1996) 11169–11186.
- [43] J.P. Perdew, K. Burke, M. Ernzerhof, Generalized gradient approximation made simple, *Phys. Rev. Lett.* 77 (1996) 3865–3868.
- [44] G. Kresse, D. Joubert, From ultrasoft pseudopotentials to the projector augmented-wave method, *Phys. Rev. B* 59 (1999) 1758–1775.
- [45] H.J. Monkhorst, J.D. Pack, Special points for Brillouin-zone integrations, *Phys. Rev. B* 13 (1976) 5188–5192.

- [46] L. Gao, Q. Fu, M. Wei, Y. Zhu, Q. Liu, E. Crumlin, Z. Liu, X. Bao, Enhanced nickel-catalyzed methanation confined under hexagonal boron nitride shells, *ACS Catal.* 6 (2016) 6814–6822.
- [47] P. Mallet-Ladeira, P. Puech, C. Toulouse, M. Cazayous, N. Ratel-Ramond, P. Weisbecker, G.L. Vignoles, M. Monthieux, A Raman study to obtain crystallite size of carbon materials: a better alternative to the Tuinstra–Koenig law, *Carbon* 80 (2014) 629–639.
- [48] S. Helveg, C. López-Cartes, J. Sehested, P.L. Hansen, B.S. Clausen, J.R. Rostrup-Nielsen, F. Abild-Pedersen, J.K. Nørskov, Atomic-scale imaging of carbon nanofibre growth, *Nature* 427 (2004) 426–429.
- [49] A. Gili, L. Schlicker, M.F. Bekheet, O. Görke, D. Kober, U. Simon, P. Littlewood, R. Schomäcker, A. Doran, D. Gaissmaier, T. Jacob, S. Selve, A. Gurlo, Revealing the mechanism of multiwalled carbon nanotube growth on supported nickel nanoparticles by in situ synchrotron X-ray diffraction, density functional theory, and molecular dynamics simulations, *ACS Catal.* 9 (2019) 6999–7011.
- [50] J.-X. Kang, D.-F. Zhang, G.-C. Guo, H.-J. Yu, L.-H. Wang, W.-F. Huang, R.-Z. Wang, L. Guo, X.-D. Han, Au catalyzed carbon diffusion in Ni: a case of lattice compatibility stabilized metastable intermediates, *Adv. Funct. Mater.* 28 (2018) 1706434.
- [51] P. Hongmanorom, J. Ashok, G. Zhang, Z. Bian, M.H. Wai, Y. Zeng, S. Xi, A. Borgna, S. Kawi, Enhanced performance and selectivity of CO₂ methanation over phyllosilicate structure derived Ni-Mg/SBA-15 catalysts, *Appl. Catal. B: Environ.* 282 (2021), 119564.